LASER & PHOTONICS REVIEWS
www.lpr-journal.org

Topology Engineering of Red Perovskite Quantum Dots Glasses: A Path to Display with Rec.2020 Standard

Shaojun Wang, Shuxin Chen, Tao Pang, Enhao Cao,* Zhehong Zhou, Sifan Zhuo, Lingwei Zeng, Jidong Lin, and Daqin Chen**

Perovskite quantum dots (PeQDs) glasses with super stability and excellent optical properties have become one of the hot candidates as color-converting materials for wide-color-gamut displays. However, it is a great challenge to simultaneously tune luminescent wavelength and photoluminescent quantum yield (PLQY) for red-emitting halogen-mixed $CsPb(Br/I)_3$ in inorganic glass matrix to completely fulfill Rec.2020 display standard. Herein, topology engineering of borosilicate glass network via controlling B_2O_3 content is demonstrated to be an effective strategy to address the issue for the first time. Molecular dynamics (MD) simulation, structural and spectroscopic characterizations evidence that appropriate B_2O_3 content enables the transition of glass network structure from 3D to 2D, which promotes I^- diffusion and in situ growth of high-quality $CsPb(Br/I)_3$ PeQDs in glass. As a result, the as-prepared $CsPb(Br/I)_3$@glass shows a record PLQY up to 91% with an ideal emitting wavelength of 645 nm and provides excellent visual effects for the constructed PeQDs-converted backlit display. This finding fills a gap in wavelength and efficiency modulation for halogen-mixed PeQDs glasses and paves the way to implement the Rec.2020 display standard.

1. Introduction

Perovskite quantum dots (PeQDs) glasses, i.e., $CsPbX_3$@glass (X = Cl, Br, I), are considered to be one of the best candidates for photoluminescent (PL) color converters in the backlit liquid crystal display (LCD) as they have super stability and retain optical properties of colloidal PeQDs, such as high color purity and large absorption cross-section.[1–6] The dense inorganic glass network provides a good 'shelter' for QDs, making QDs@glass bring substantial progress in practical applications.[7–11] However, high-quality displays have strict requirements on emitting efficiency and wavelength of color converters.[12–14] Therefore, the development of $CsPbX_3$@glass with high PL quantum yield (PLQY) and suitable wavelength has become a hot topic in the present research.

Currently, pure green $CsPbBr_3$@glass with ≈530 nm emission and 94% PLQY under the "accumulation" effect of Zr^{4+} in borosilicate glass has been developed to satisfy the requirement of the Rec.2020 green light standard.[15] However, compared with the green $CsPbBr_3$@glass, the pure $CsPbI_3$@glass shows a deep-red emission with a wavelength greater than 670 nm, which does not meet the requirements of the red wavelength (620–650 nm) for high-definition display.[9,16–20] In recent years, researchers have made a great effort to improve the optical performance of $CsPbI_3$@glass, including modulation of perovskite components, modification of glass network structures, and optimization of in situ glass crystallization conditions (Table S1, Supporting Information). Among them, I^- ions alloying to produce $CsPb(Br/I)_3$@glass is an effective way to obtain red-emitting PeQDs with wavelength shorter than 650 nm but suffers from low PLQY owing to the

S. Wang, S. Chen, T. Pang, Z. Zhou, S. Zhuo, J. Lin, D. Chen
College of Physics and Energy
Fujian Provincial Key Laboratory of Quantum Manipulation and New Energy Materials
Fujian Normal University
Fuzhou 350117, P. R. China
E-mail: 02009@zjhu.edu.cn; dqchen@fjnu.edu.cn

T. Pang
Huzhou Key Laboratory of Materials for Energy Conversion and Storage
College of Science
Huzhou University
Huzhou, Zhejiang 313000, P. R. China

E. Cao
College of Materials Science and Engineering
Kunming University of Science and Technology
Kunming 650093, P. R. China
E-mail: caoenhao@kust.edu.cn

L. Zeng
School of Chemistry and Chemical Engineering
Key Laboratory of Theoretical Organic Chemistry and Functional Molecule of Ministry of Education
Hunan University of Science and Technology
Xiangtan 411201, P. R. China

D. Chen
Fujian Provincial Engineering Technology Research Center of Solar Energy Conversion and Energy Storage
Fuzhou, Fujian 350117, P. R. China

The ORCID identification number(s) for the author(s) of this article can be found under https://doi.org/10.1002/lpor.202500550

DOI: 10.1002/lpor.202500550

unbalanced halogen (Br&I) diffusion in glass network and the resulted defect quenching centers.[21–25] Therefore, how to assist the appropriate amount of Br&I in the perovskite lattice without the formation of non-radiative recombination centers is the key factor in improving the optical performance of $CsPb(Br/I)_3$@glass.

In general, the diffusion behaviors of Br^- and I^- ions in the "reaction solvent" (i.e., glass matrix) are limited by the topology network structure of glass,[26,27] and the related diffusion mechanism is ambiguous and has not been well understood so far. In this work, we first adopted molecular dynamics (MD) simulation to explore the influence of B_2O_3 concentration on the topology structure of borosilicate glass. It is found that the topology of the glass network shows a transition from 3D to 2D with an increase of B_2O_3 content, which in turn enhances the diffusion rate of I^- ions in glass and is beneficial for the incorporation of I^- into $CsPbBr_3$ lattice without inducing defects. As a result, we then successfully prepared the I-rich $CsPb(Br/I)_3$@glass with a record PLQY of 91% at 645 nm emission. In particular, the emitting wavelength can be finely tuned within 620–650 nm without an obvious decline of PLQY (Table S1, Supporting Information), which meets the strict requirements of Rec.2020 for red primary color. This work fills a gap in wavelength and efficiency modulation for red-emitting halogen-mixed $CsPb(Br/I)_3$@glass and paves the way for the realization of a backlit display with the Rec.2020 standard.

2. Results and Discussion

Precisely controlling Br&I concentration and ratio in the perovskite lattice is the key to preparing $CsPb(Br/I)_3$@glass composites with ideal optical performance. Currently, the borosilicate glasses have been commonly used as the hosts to accommodate $CsPb(Br/I)_3$ PeQDs. Notably, B_2O_3 exists in the glass network structure in the form of $[BO_3]$ and $[BO_4]$, which has a significant impact on the glass structure and subsequent in situ nucleation/growth of PeQDs. Herein, MD simulation was conducted to explore the influence of B_2O_3 concentration on the glass network structure and PeQD crystallization. The glasses with the compositions of xB_2O_3-$75SiO_2$-$7ZnO$-$3CaF_2$-$10Cs_2CO_3$-$1PbBr_2$-$1PbI_2$-5NaBr-5NaI (where x = 55, 75, 110, labeled as M1, M2 and M3, respectively) were designed. A total of 100,000 atoms were randomly packed into a 60 nm × 60 nm × 3 nm slice cell with the corresponding nominal molar ratio using PACKMOL, and the related processes, including glass melting, glass quenching, and glass re-heating to induce nucleation/growth of $CsPb(Br/I)_3$ PeQDs in glass, were simulated (Experimental Section in SI). **Figure 1**a–c exhibits MD simulation results of glass network configurations. As shown in Figure S1 (Supporting Information), the Si—O bond length remains 0.161 nm by analyzing the radial distribution functions (RDFs) of M1, M2, and M3, which is consistent with the experiment results.[28,29] For the B—O bond, the RDF shows double peaks at 0.137 nm and 0.147 nm, which are attributed to $[BO_3]$ and $[BO_4]$,[30,31] respectively. Importantly, as the B_2O_3 content increases, the peak corresponding to the B—O bond in $[BO_3]$ becomes more prominent, indicating an increased proportion of $[BO_3]$ units related to $[BO_4]$ ones. This leads to an increased volume expansion rate from M1 to M3 when elevating the temperature of samples (Figure S2a,b, Supporting Information). This is due to the increase in $[BO_3]$ units, resulting in a 2D network structure with a higher coefficient of thermal expansion. Therefore, increasing B_2O_3 content in the glass can convert a 3D glass network structure into a 2D one, which subsequently leads to a decrease in the structural compactness of the glass.

As evidenced in Figure 1d–f, the local magnification images for the M1, M2, and M3 samples after heat treatment at 845 K show the orderly arrangement of Cs, Pb, Br and I elements in the glass network, indicating successful crystallization of $CsPb(Br/I)_3$ PeQDs in glass. Detailed RDF analyses of the heat-treated samples show that all three M1-M3 samples exhibit a prominent second peak in their RDF curves (Figure 1g–i), providing conclusive evidence of in situ growth of $CsPb(Br/I)_3$ PeQDs in glass.[32,33] Further analysis of the RDF of Pb-I shows that the second peak intensity of M3 is more significant than those of M2 and M1 (Figure S3, Supporting Information), indicating that the M3 sample has superior crystallinity of PeQDs. These findings suggest that the addition of high-content B_2O_3 has a positive effect on the crystallization process of PeQDs. As revealed in Figure S2c (Supporting Information), adding high-content B_2O_3 promotes all the ionic migration in the glass owing to the conversion of glass structure from 3D to 2D. However, the increased migration capacity of I^- ions is higher than that of Br^- ones. As a consequence, it is found that the proportion of I^- ions related to Br^- ones enhances with an increase of B_2O_3 content based on a statistical analysis of the Br&I contents in the crystallized region (Figure S2d, Supporting Information). In addition, the Br/I ratios in different crystalline regions within M1 exhibit significant variations, whereas those in M2 and M3 gradually converge in different crystalline regions (Figure S4, Supporting Information). This phenomenon is ascribed to the increased proportion of $[BO_3]$ units, which induces a transition in the glass network topology toward a 2D structure. This transition not only reduces the diffusion barrier for I^- ions, thereby enhancing their diffusion rate but also results in a uniform Br-to-I ratio across different crystalline regions within the glass, thus facilitating the homogeneous growth of PeQDs.

Based on MD simulations, we further conducted experimental validations to explore the impact of B_2O_3 content on glass network structure and optical performance of hybrid halogen PeQDs glasses. As tabulated in Table S2 (Supporting Information), a series of $CsPb(Br/I)_3$@glasses with different B_2O_3 contents (55–110 mol%) were prepared by a melt-quenching method and subsequent in situ crystallization at (Experimental Section in Figure S5, Supporting Information). To determine the effect of the proportion of $[BO_3]$ units on the uniformity of the Br/I perovskite phase, all the samples are heat-treated at the same temperature and time (570 °C for 2 h). As illustrated in **Figure 2**a, PL of $CsPb(Br/I)_3$@glass exhibits a gradual change from a composite broadband yellow light to a narrowband red light with an increase of B_2O_3 content; meanwhile, the absorption shoulder gradually red-shifts, and the calculated optical bandgap decreases from 2.35 to 1.92 eV (Figure 2b; Figure S6 and Table S3, Supporting Information). It is clearly observed that the low-content B_2O_3 samples exhibit a yellow color, which gradually converts into a bright red one with a rise of B_2O_3 content (Figure 2c). Upon UV light excitation, the luminescent color changes from yellow-orange to bright

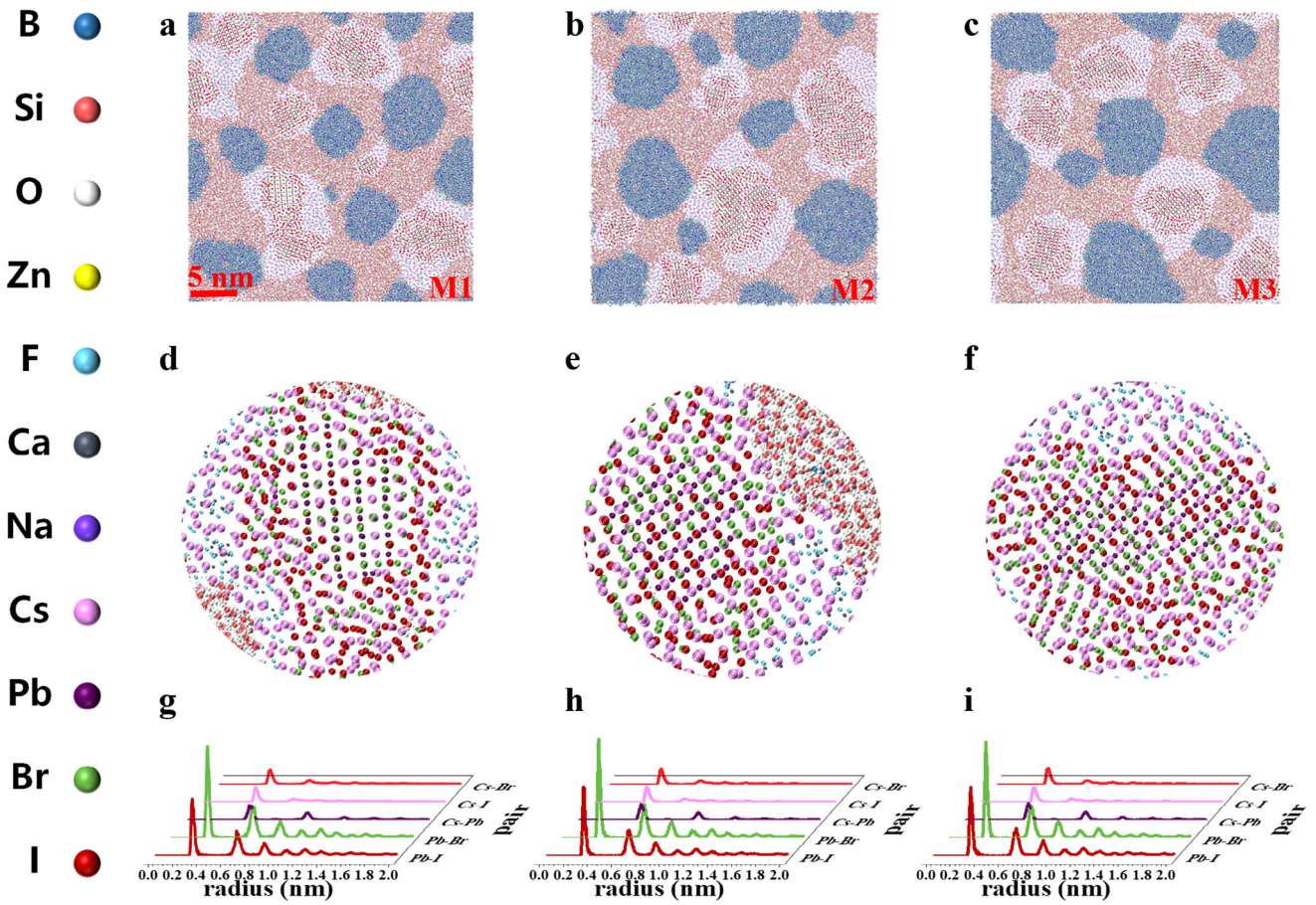

Figure 1. a–c) MD simulation of glass network configurations, d–f) crystalline regions and g–i) RDFs for the $CsPb(Br/I)_3$@glass samples with different B_2O_3 concentrations.

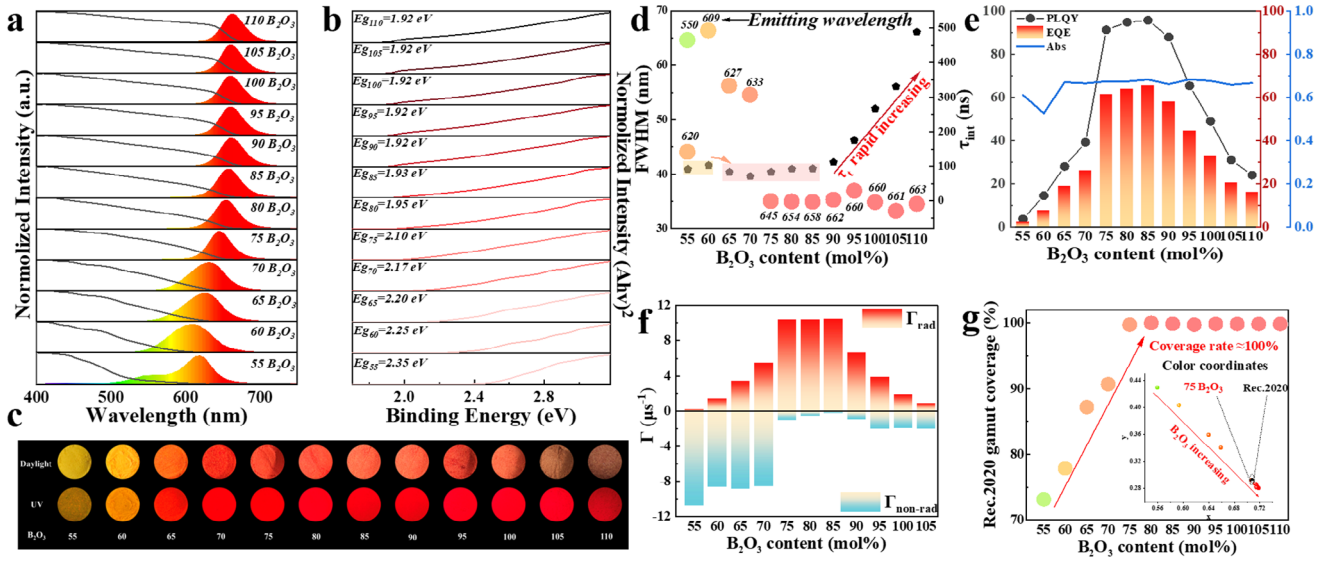

Figure 2. a) Absorption/PL spectra and b) $(Ahv)^2$ versus energy to calculate optical bandgap, c) photographs of the $CsPb(Br/I)_3$@glass powders prepared with different B_2O_3 contents, d) FWHM & emission peak wavelength & PL decay lifetime, e) PLQY & EQE & Absorption efficiency, f) radiative and non-radiative rates, and g) color coordinates of PL spectra obtained from the $CsPb(Br/I)_3$@glass nanocomposites with different B_2O_3 contents.

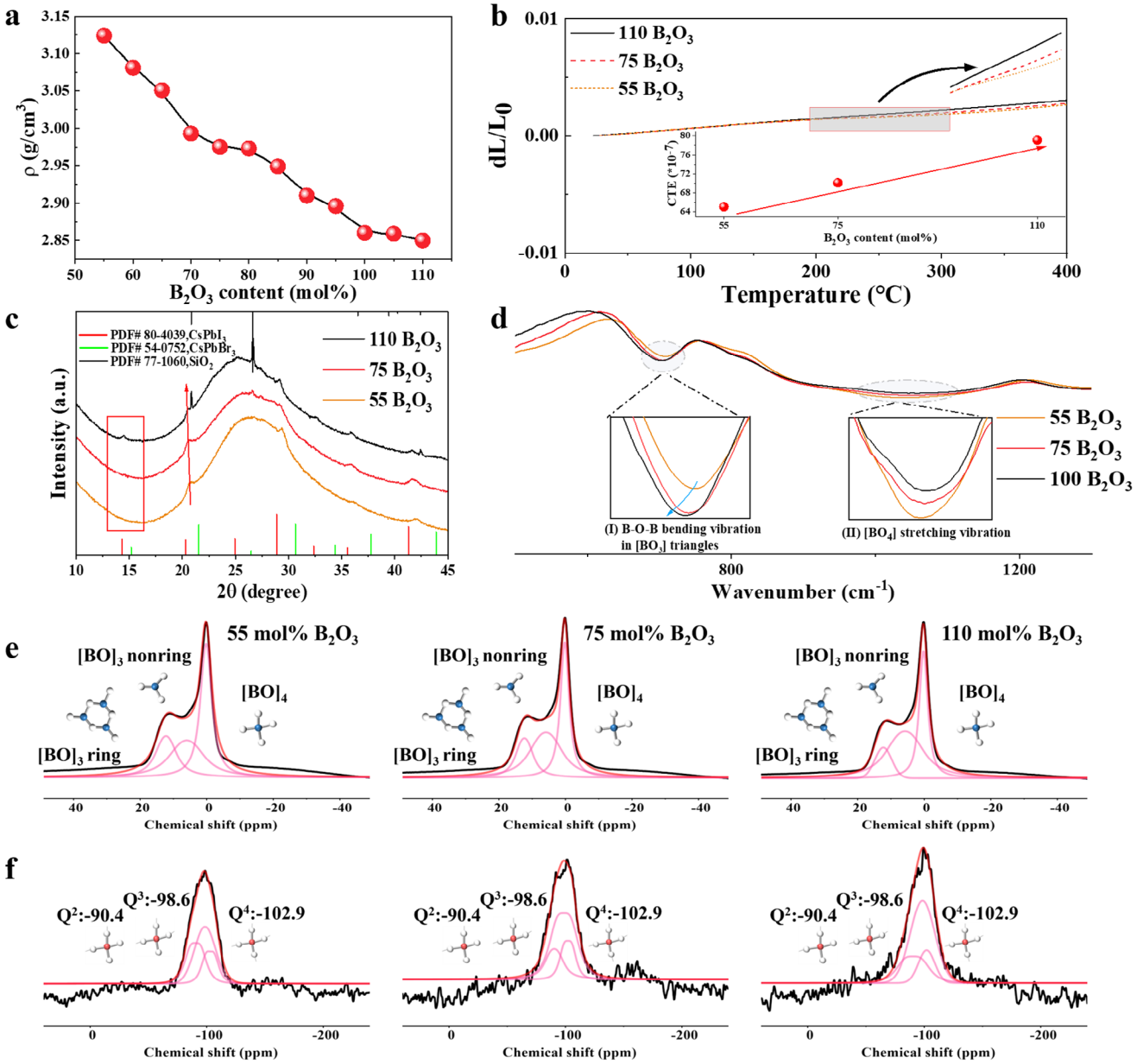

Figure 3. a) Dependence of density (ρ) and, b) expansion coefficient on B_2O_3 content. c) XRD patterns, d) FTIR spectra, e) ^{11}B, and f) ^{29}Si MAS-NMR spectra (black line) and the fitted results (red line: sum; pink lines: components) for the $CsPb(Br/I)_3$@glass with different B_2O_3 contents.

red, and finally to deep red (Figure 2c). PL spectra show that the 55 B_2O_3 sample has two emitting centers with distinct green (550 nm) and red (620 nm) components, leading to a large full width at half maximum (FWHM) of 65.3 nm. With the increase of B_2O_3 content, the green emitting component disappears and the red one remains, followed by the red luminescence red-shifting from 620 nm to ≈660 nm, and the FHWM decreases down to 35 nm (Figure 2d). PL decay lifetimes of the $CsPb(Br/I)_3$@glass samples with 55–90 mol% B_2O_3 are about ≈100 ns and then rapidly rise up to ≈500 ns with further increase of B_2O_3 content (Figure 2d; Table S4, Supporting Information). All the samples have high absorption coefficients of ≈70%, and their PLQYs & external quantum efficiencies (EQEs) tend to enhance with an increase of B_2O_3 content and then decline when the B_2O_3 content exceeds 85. The best PLQY&EQE reach as high as 91 and 61%, 93 and 63%, and 95 and 66% for the $CsPb(Br/I)_3$@glass samples with 75, 80, and 85 mol% B_2O_3, respectively (Figure 2e). Accordingly, these samples have high radiative recombination rates and low non-radiative rates (Figure 2f). As tabulated in Table S1 (Supporting Information), the PLQY values of the samples with 75–85 mol% B_2O_3 are the highest ones for the $CsPb(Br/I)_3$@glass composites reported so far. As revealed in Figure 2g, the color coordinates of the samples gradually approach the Rec.2020 standard with an increase of B_2O_3 content and the color gamut coverage accordingly increases and reaches ≈100% for the samples when the B_2O_3 content is above 70 mol%. Specifically, for the sample with

75 mol% B_2O_3, its emission wavelength of 645 nm, color coordinates of (0.706, 0.292), color gamut up to 99.68%, PLQY&EQE of 91 and 61%, and FWHM of 35 nm, can totally meet the requirement of the Rec.2020 red primary color standard for backlit display.

To find out the influence of B_2O_3 content on the topology structure of the borosilicate glass network, we make a series of characterizations from macroscopic to microscopic points of interest. As illustrated in **Figure** 3a,b and Table S5 (Supporting Information), the density of borosilicate glass decreases from 3.12 to 2.85 g cm^{-3} and the coefficient of thermal expansion (CTE) of the glass gradually increases with the increase of B_2O_3 content, which is consistent with the results of MD simulation (Figure S2a,b, Supporting Information). This is mainly due to the increase in the number of $[BO_3]$ groups and thus conversion of 3D glass network structure into 2D one, which subsequently leads to a decrease in the structural compactness of the glass. This alteration, in turn, triggers a decrease in density and an increase in CTE. When the temperature is approaching the crystallization of one of the PeQDs in glass, the high expansion conditions make the softened glass sufficiently loose to lower the migration barrier for the perovskite elements. Transmission electron microscopy (TEM) images have definitely demonstrated a progressive increase in the number and size of PeQDs with an increase of B_2O_3 content (Figure S7, Supporting Information), primarily attributing to the alteration of the glass topology structure. Taking $CsPb(Br/I)_3$@glass sample with 85 mol% B_2O_3 as a typical example, high-angle annular dark-field (HAADF) scanning TEM (HAADF-STEM) image and elemental mapping confirms that the PeQDs in glass are of uniform size and have a homogeneous elemental distribution (Figure S8, Supporting Information). Further in-depth analysis of X-ray diffraction (XRD) patterns indicates that the addition of high-content B_2O_3 facilitates the migration of I^- ions, enabling a greater number of I^- ions to actively participate in the lattice construction process. This is evidenced by the shift of the diffraction peak angle from 20.69° to 20.52° (Figure 3c; Figure S9a,b, Supporting Information). Additionally, the incorporation of high-content B_2O_3 also favors the precipitation of PeQDs, as demonstrated by significant enhancement of diffraction peak intensities within the boxed region of XRD patterns (Figure 3c). It is noteworthy that a distinct diffraction peak attributable to silica becomes clearly observable in the XRD patterns (Figure 3c; Figure S9b, Supporting Information). As B_2O_3 content gradually elevates, the number of $[BO_3]$ within the glass intensifies, fostering the development of boron-rich and silica-rich phases, which in turn exacerbates phase separation within the glass and results in the precipitation of SiO_2 crystals.

Fourier transform infrared (FTIR) spectra and Raman spectra reveal significant alteration of the borate groups in the borosilicate glass. With the increase of B_2O_3 content, the B—O—B bending vibration of the $[BO_3]$ triangle located at 704 cm^{-1} increases, the B—O—B stretching vibration of the $[BO_4]$ unit at 1404 cm^{-1} decreases (Figure 3d), and the $[BO_3]$ Raman peak located at 900 cm^{-1} is clearly prominent (Figure S10, Supporting Information).[34] All these results confirm that the relative content of $[BO_3]$ units in the glass network structure increases and a 2D glass network topology is produced for the samples with high-content B_2O_3. To validate the modification of the glassy network structure, magic angle spinning nuclear magnetic resonance (MAS-NMR) spectra of ^{11}B and ^{29}Si were further recorded (Figure 3e,f). Each ^{11}B MAS spectrum has been deconvoluted into three peaks of $^{[3]}B$(ring), $^{[3]}B$(nonring), $^{[4]}B$ and ^{29}Si spectrum can be deconvoluted into three peaks of Q^2, Q^3, and Q^4 using the Gaussian peak shape function.[35,36] The corresponding NMR decomposition results and relative percentages of each species are summarized in **Table 1**. With the increase of B_2O_3 content, more $^{[3]}B$(ring) and $^{[4]}B$ units are converted into $^{[3]}B$(nonring) ones, and more Q^4 unit is converted into Q^3 ones. These findings indicate that high-content B_2O_3 in glass destructs the network connectivity of $[BO_4]$&$[SiO_4]$ by the partial conversion of them into $^{[3]}B$(nonring)& Q^3 with the release of free oxygen acting as a bond breaker. To support this view, high-resolution X-ray photoelectron spectroscopy (XPS) data of B 1s, Si 2p, and O 1s for the samples with 55, 75, and 110 mol% B_2O_3 were recorded (Figure S11, Supporting Information). The B 1s signal deconvoluted into two components at 192.2 and 192.6 eV is ascribed to B bonding in the $[BO_3]$ and $[BO_4]$ units, respectively (Figure S11a, Supporting Information), and the Si 2p signal is decomposed into three components at 101.7, 102.4, and 103.2 eV, corresponding to Q2, Q3, and Q4 units, respectively (Figure S11b, Supporting Information), which also show a tendency of increase of $[BO_3]$ and Q3 structural units and decrease of $[BO_4]$ and Q4 structural units with increase of B_2O_3 content. The O 1s signal is deconvoluted into two components at 531.4 eV and 532.1 eV, assigning to non-bridged oxygen (NBO) and bridged oxygen (BO),[37,38] respectively (Figure S11c, Supporting Information). Obviously, with an increase of B_2O_3 content, the proportion of NBO gradually enhances. As a result, with an increase of B_2O_3 content, the Br 3d signal gradually increases owing to the release of Br from Pb—Br bonding in PeQDs, while the I 3d binding energy moves to low energy, indicating that more I^- ions are involved in the PeQD lattice (Figure S12, Supporting Information). The results are consistent with MD simulations shown in Figure S4 (Supporting Information) and PL spectra data shown in Figure S13 (Supporting Information). Therefore, it can be concluded that the addition of high-content B_2O_3 makes the glass network convert from a compact 3D structure into a sparse 2D one. The 3D glass network structure hinders the migration of I^- ions and inhibits the formation of high-quality $CsPb(Br/I)_3$ PeQDs in glass. Conversely, increasing the number of 2D layered $^{[3]}B$(nonring)

Table 1. The decomposition data form the ^{11}B and ^{29}Si NMR spectra. δ_{iso} represents a chemical shift. Q^n denotes quaternary silicon, where the superscript n = 2–4 indicates the number of bridging oxygens. ^3B and $^3B_{non}$ are defined as the triangle BO_3 group forming a ring or not, and ^4B represents the tetrahedral BO_4 group.

Elements	Species	δ_{iso} [ppm]	55	75	110
				area (%)	
^{11}B	^3B	12.3	23.2	19.8	12.0
	$^3B_{non}$	6.0	33.8	42.6	52.6
	^4B	0.2	43.0	37.6	35.4
^{29}Si	Q^2	−90.4	32.3	22.1	24.9
	Q^3	−98.6	46.1	58.5	59.4
	Q^4	−102.9	21.6	19.4	15.7

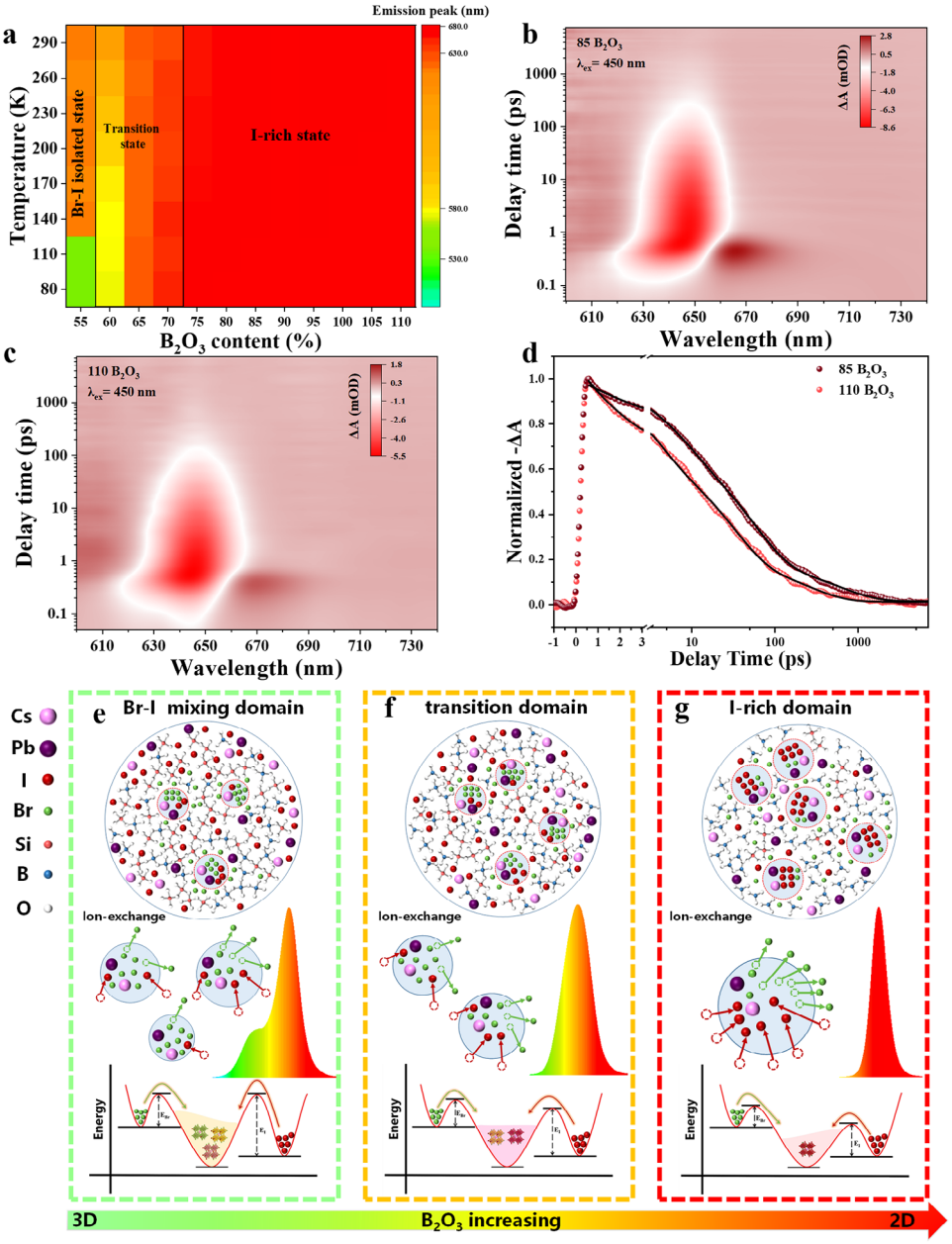

Figure 4. a) Temperature-dependent PL mapping for the $CsPb(Br/I)_3$@glass samples with various B_2O_3 contents. Pseudo-color TA spectra of $CsPb(Br/I)_3$@glass samples with b) 85 mol% B_2O_3, c) 110 mol% B_2O_3, and d) the corresponding bleach recovery kinetic curves upon 450 nm fs laser excitation. Schematic thermodynamics of the effect of glass topology structure on Br&I ionic exchange in the $CsPb(Br/I)_3$@glass: e) Br-I mixing domain, f) transition domain, g) I-rich domain.

and ^3Q structural units promotes the diffusion of I^- ions, allowing more I^- ions to participate in the $CsPb(Br/I)_3$ perovskite lattice.

To investigate the effect of borosilicate glass topology structure on the formation of hybrid halogen PeQDs, we performed temperature-dependent spectroscopic tests on the samples with various B_2O_3 contents. As illustrated in Figure S13 (Supporting Information) and **Figure** 4a, we classified all the samples into three kinds of states: Br-I isolated state (55 mol% B_2O_3), transition state (60–70 mol% B_2O_3), and I-rich state (75–110 mol% B_2O_3). In the Br-I isolated state, two emission peaks appear distinctly with a decrease of temperature and show significant differences of decay lifetimes (30.6 ns &91.7 ns, Figure S14, Supporting Information), verifying that borosilicate glasses with low-content B_2O_3 are vulnerable to the formation of polymorphic emissions from hybrid halogen PeQDs in the glass. During the change from the transition state (60–70 mol% B_2O_3) to the I-rich state (75–110 mol% B_2O_3), a notable phenomenon is the gradual redshift of peak one, the boundary between peak one and peak two becomes blurred, and eventually they merge to pro-

duce an individual red emitting band (Figure 4a). However, the luminescence performance decreases significantly for the samples with high B_2O_3 contents (90–110mol%, Figure 2e). To explore the influence of B_2O_3 content on the carrier trapping and exciton recombination, femtosecond transient absorption (*fs*-TA) spectra were recorded to study the ultrafast relaxation process of excitons in the $CsPb(Br/I)_3$@glass samples with 85 and 110 mol% B_2O_3, respectively. The pseudo-color TA spectra of both samples at various delay times present typical ground-state bleaching signals (Figure 4b,c), and their bleaching peak data were extracted for triple-exponential fitting (Figure 4d), where the three processes can be assigned to shallow trap (τ_1), deep trap (τ_2), and carrier radiative recombination (τ_3), respectively.[39,40] The three components τ_1, τ_2, and τ_3 of 85 mol% B_2O_3 based sample are 7.19 ps, 56.50 ps, and 655.66 ps, and those of 110 mol% B_2O_3 based sample are 3.03 ps, 31.03 ps, and 278.05 ps, respectively. The notably shorter lifetimes in 110 mol% B_2O_3 indicate faster carrier decay, likely due to higher trap densities. This confirms that excessive B_2O_3 incorporation leads to the precipitation of PeQDs with more defects. This may be attributed to the overgrowth of PeQDs accompanied with vacancy defects and interface defects between PeQD and glass matrix. Following that, we did several sets of heat treatments by controlling crystallization temperature and duration on the samples with different B_2O_3 contents (Figure S15, Supporting Information). It is concluded that the glassy network structure with high-content B_2O_3 is indeed able to lower the potential barrier for the growth of $CsPb(Br/I)_3$ PeQDs in glass with an individual red emission, even when the external crystallization conditions are not sufficiently supplied.

Therefore, based on MD simulations and experimental data, it is believed that the formation of hybrid halogen $CsPb(Br/I)_3$ PeQDs in borosilicate glass is highly dependent on the glass topology structure, which significantly affects the diffusion of Br&I ions. High-content B_2O_3 enables the conversion of glass network structure from 3D to 2D, which promotes the precipitation of the $CsPb(Br/I)_3$ perovskite phase with an ideal emission wavelength of 645 nm and PLQY up to 91%. As illustrated in Figure 4e–g, the nucleation/growth occurs during the heat treatment process and encompasses the phase separation process of perovskite elements from the glass matrix and the subsequent halogen ionic exchange between the phase separation region and the glass matrix. The diffusion behavior of perovskite elements in glass during phase separation follows the Arrhenius model, which is expressed as[41]

$$\nu = \nu_0 \exp\left(-E_D/kT\right) \quad (1)$$

where ν denotes the attempt frequency and E_D is the diffusion barrier affected by the glass topology. Compared with the I^- ion, the Br^- ion has a smaller size and a lighter mass, and its migration rate is usually higher than that of the I^- ion under thermal drive, enabling the Br^- ion to cross the potential barrier of the glass matrix more rapidly and achieve kinetically preferential activation. In addition, the strong complexation affinity between Br^- and Pb^{2+} further promotes the formation of Br-rich halide regions.[42] Subsequently, driven by the concentration gradient, I^- ions enter the Br-rich halide region and exchange with Br^- ions, but they are limited by the compact 3D glass structure. Therefore, the I-rich region is not yet fully formed, and the Br-rich region is not completely disappeared, resulting in the formation of polymorphic emissions for the Br-I isolated state (Figure 4e). With the increase of B_2O_3 content, the glass network undergoes a gradual alteration from the original 3D structure to 2D one, which significantly increases the diffusion rate of I^- ions and reduces their migration barriers. Then, the concentration gradient drives more I^- ions to overcome the kinetic diffusion barrier (E_D) and enter the Br-rich region via an ionic exchange reaction. Under this condition, a large amount of I^- ions is incorporated into the perovskite lattice, leading to a significant red-shifting and narrowing of the emission band and finally the formation of the I-rich region (Figure 4f,g). To demonstrate the versatility of the proposed mechanism, we extended the experimental study to the $CsPb(Cl/Br)_3$@glass system. Indeed, as B_2O_3 content increases, similar phenomena, including red-shifting and narrowing of emission, are observed, owing to the lowered diffusion barrier of Br^- ions relative to Cl^- ions in glass (Figure S16, Supporting Information).

Benefited from glass topology engineering induced red $CsPb(Br/I)_3$@glass (75 mol% B_2O_3) with average size of ≈23 nm (Figure S7b, Supporting Information), an emission wavelength of 645 nm and PLQY up to 91%, it is highly suitable to construct wide-color-gamut backlit display to satisfy Rec.2020 standard. First, we conducted a series of stability tests on the $CsPb(Br/I)_3$@glass. As presented in Figure S17a (Supporting Information), the sample exhibits excellent thermal reversibility after three-time heating/cooling cycles between 290 K and 470 K, without significant change in PL intensity. In addition, after 1,800 h of harsh commercial 85 °C/85%RH accelerated aging and 450 nm blue light irradiation, the sample demonstrates excellent durability, retaining 87.3% and 84.9% of PL intensity (Figure S17b, Supporting Information). The super long-term stability of red $CsPb(Br/I)_3$ is attributed to the well-protection of PeQDs by the robust glass matrix. Then, yellow PeQDs enhanced film (PQDF) was prepared by mixing the as-fabricated red $CsPb(Br/I)_3$@glass and green $CsPbBr_3$@glass with polydimethylsilane (PDMS). As shown in **Figure 5**a, a white light backlight unit is designed by coupling the yellow PQDF with a blue light guide panel (LGP) and covering it with a brightness enhancement film (BEF) and a dual brightness enhancement film (DBEF). Under the driving voltage/current of 12 V/300 mA, the PQDF-based backlight unit produces bright white light (Figure 5b). We successfully constructed an 8.9-inch LCD prototype device by combining the PQDF-based white light backlight unit with a commercial TFT-LCD panel (Figure 5c). Compared to commercial YAG: Ce LCD, the FWHMs of the $CsPbX_3$@glass (green/red: 19/32 nm, Figure 5d) are far narrower than those of YAG: Ce rare-earth phosphors (67/47 nm, Figure 5e). After testing, under the excitation of blue light with the same power, the output light intensities of the 9 randomly selected test points of PQDF are highly consistent, proving that it has excellent light output uniformity (Figure S18, Supporting Information). By analyzing the images displayed on commercial LCD and PQDF-based ones, we can intuitively observe the differences in color rendering performance. Specifically, the PQDF-based display exhibits more saturated and realistic red and green

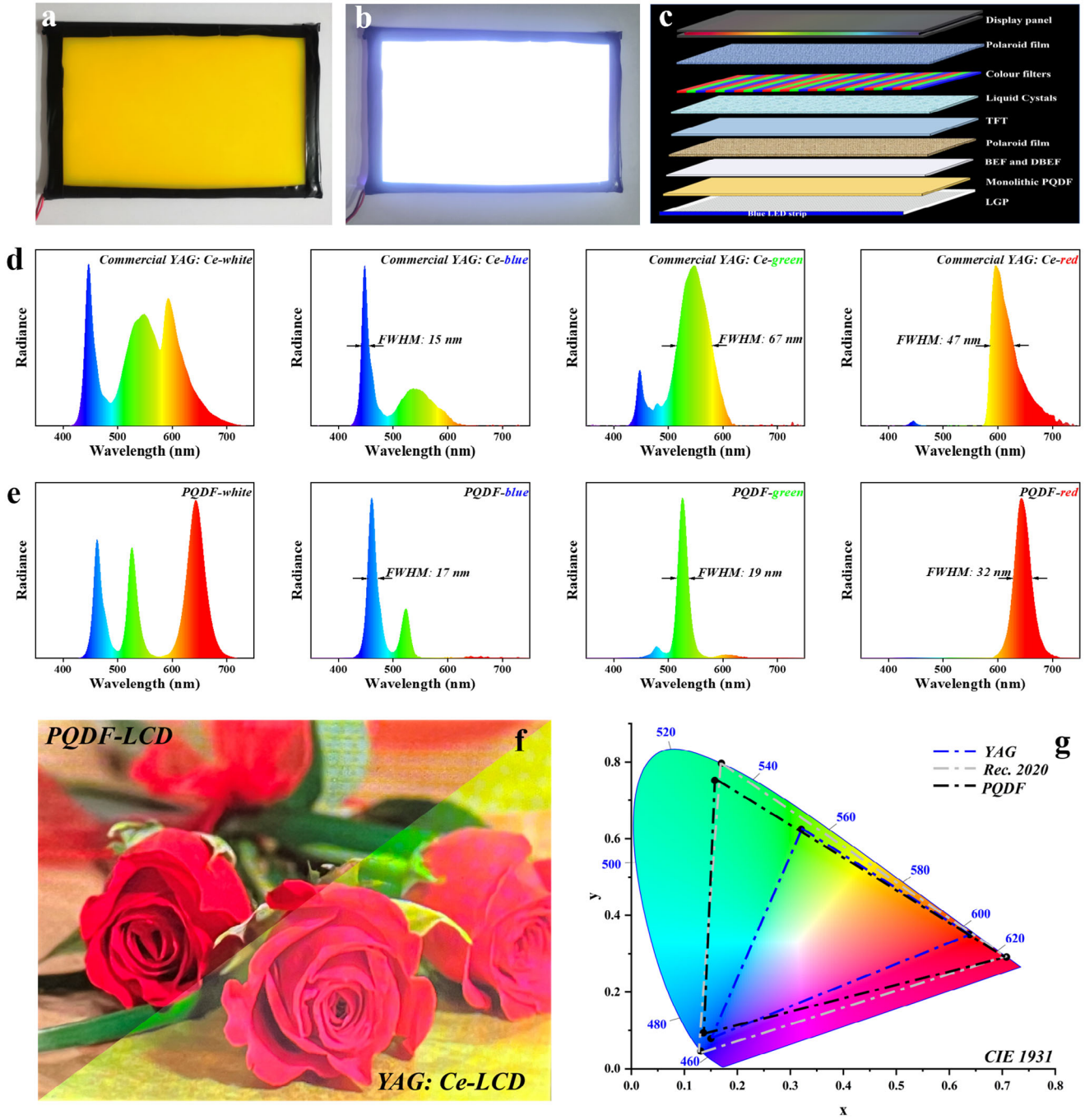

Figure 5. a) Photograph of a yellow monolithic PQDF-based backlit unit and b) its luminescent image at an operating voltage of 12 V. c) Schematic structure of an LCD prototype using yellow PQDF as a light converter. PL radiation spectra of white, blue, green, and red images directly recorded from d) the YAG-based LCD and e) the PQDF-based LCD. f) Comparison of the display performance of the YAG-based LCD and the PQDF-based LCD. g) Color gamut of YAG-based commercial LCD (blue triangle), PQDF-based LCD (black triangle), and Rec.2020 standard (gray triangle).

hues, in stark contrast to the yellowish-green tones and poorer color rendering performance of the YAG-based commercial display (Figure 5f; Figure S18, Supporting Information). This is attributed to the ultra-wide color gamut of the PQDF-based LCD (Figure 5g), which reaches 88% (after color filters) of the Rec.2020 standard and is much higher than that of the YAG: Ce-based LCD (52%).

3. Conclusion

In summary, topology engineering of borosilicate glass network via modifying B_2O_3 content has been developed to achieve a 3D-to-2D glass structure transition. This brings about a decrease in the migration barrier of I^- ions and enables in situ growth of high-quality halogen-mixed $CsPb(Br/I)_3$ PeQDs in a glass ma-

trix. Therefore, the as-prepared red-emitting $CsPb(Br/I)_3$@glass shows superior optical performance, including 645 nm emission wavelength, a record PLQY above 90%, and outstanding long-term stability, to totally satisfy the Rec.2020 display standard. Finally, we constructed a prototype LCD using $CsPb(Br/I)_3$@glass as a red color converter, which can present display images with a wide color gamut of 88% Rec.2020 standard and more realistic color rendition of objects. This work will provide new ideas for wavelength tuning and efficiency enhancement of hybrid halogen perovskite quantum dots glasses and pave the way for the realization of their practical application in backlit displays.

Supporting Information

Supporting Information is available from the Wiley Online Library or from the author.

Acknowledgements

S.J.W. and S.X.C. contributed equally to this work. This research was supported by the National Natural Science Foundation of China (52272141), and the Natural Science Foundation of Fujian Province (2024J02014).

Conflict of Interest

The authors declare no conflict of interest.

Data Availability Statement

Research data are not shared.

Keywords

borosilicate glass, $CsPbX_3$, display, luminescent materials, quantum dots

Received: March 11, 2025
Revised: May 21, 2025
Published online:

[1] W. Zhu, S. Cheng, E. Mei, Y. He, J. Yang, R. Liu, X. Liang, W. Xiang, *Adv. Funct. Mater.* **2024**, *34*, 2408760.
[2] S. Chen, J. Lin, S. Zheng, Y. Zheng, D. Chen, *Adv. Funct. Mater.* **2023**, *33*, 2213442.
[3] K. Sun, D. Tan, X. Fang, X. Xia, D. Lin, J. Song, Y. Lin, Z. Liu, M. Gu, Y. Yue, J. Qiu, *Science* **2022**, *375*, 307.
[4] J. Huang, Z. Li, Y. Zhu, L. Yang, X. Lin, Y. Li, Y. Wang, Y. Wang, Y. Fu, W. Xu, M. Huang, D. Li, A. Pan, *Adv. Mater.* **2024**, *36*, 2409025.
[5] X. Fan, S. Wang, X. Yang, C. Zhong, G. Chen, C. Yu, Y. Chen, T. Wu, H. Kuo, Y. Lin, Z. Chen, *Adv. Mater.* **2023**, *35*, 2300834.
[6] Y. Liu, S. Yang, X. Luo, Z. Long, E. Cao, J. Li, Y. Chen, Q. Wang, Y. Yang, C. Wang, Y. Gao, J. Qiu, D. Zhou, *Chem. Eng. J.* **2023**, *470*, 144383.
[7] S. Liao, Z. Yang, J. Lin, S. Wang, J. Zhu, S. Chen, F. Huang, Y. Zheng, D. Chen, *Adv. Funct. Mater.* **2023**, *33*, 2210558.
[8] Y. Ma, X. Li, L. Wu, C. Shao, B. Zhang, T. Pang, L. Lu, H. Qiu, Y. Tian, G. Wang, Y. Hui, Q. Guo, D. Chen, *J. Adv. Ceram.* **2024**, *13*, 354.
[9] J. Li, D. Zhou, Y. Liu, Y. Chen, J. Chen, Y. Yang, Y. Gao, J. Qiu, *ACS Appl. Mater. Interfaces* **2023**, *15*, 22219.
[10] J. Lin, S. Chen, W. Ye, Y. Zeng, H. Xiao, T. Pang, Y. Zheng, B. Zhuang, F. Huang, D. Chen, *Adv. Funct. Mater.* **2024**, *34*, 2314795.
[11] Z. Yang, S. Zheng, G. Xi, T. Pang, S. Wang, Q. Ye, B. Zhuang, D. Chen, *J. Adv. Ceram.* **2023**, *12*, 2075
[12] K. Ren, J. Hu, C. Bi, S. Wei, X. Wang, N. H. De Leeuw, Y. Lu, M. Sui, W. Wang, *ACS Mater. Lett.* **2024**, *6*, 4115.
[13] M. Xie, J. Guo, X. Zhang, C. Bi, L. Zhang, Z. Chu, W. Zheng, J. You, J. Tian, *Nano Lett.* **2022**, *22*, 8266.
[14] Y. Wang, W. Tang, C. Zhang, M. S. Molokeev, H. Ming, Y. Zhou, S. Peng, E. Song, Q. Zhang, *Adv. Funct. Mater.* **2024**, *34*, 2313490.
[15] S. Chen, J. Lin, J. Huang, T. Pang, Q. Ye, Y. Zheng, X. Li, Y. Yu, B. Zhuang, D. Chen, *Adv. Funct. Mater.* **2024**, *34*, 2309293.
[16] P. Li, W. Xie, W. Mao, Y. Tian, F. Huang, S. Xu, J. Zhang, *J. Alloys Compd.* **2020**, *817*, 153338.
[17] X. Li, K. Sun, J. Wu, Y. Liu, L. Li, Z. Xiao, Z. Li, X. Liu, B. Xu, J. Qiu, D. Tan, *Laser Photonics Rev.* **2024**, *18*, 2301244.
[18] C. Yi, G. Zhang, R. Lu, Z. Wang, Y. Wang, X. Cao, K. Ni, N. Chen, G. Zheng, W. Huang, J. Wang, *Nano Lett.* **2024**, *24*, 10196.
[19] J. Zhang, B. Cai, X. Zhou, F. Yuan, C. Yin, H. Wang, H. Chen, X. Ji, X. Liang, C. Shen, Y. Wang, Z. Ma, J. Qing, Z. Shi, Z. Hu, L. Hou, H. Zeng, S. Bai, F. Gao, *Adv. Mater.* **2023**, *35*, 2303938.
[20] Q. Chen, B. Tang, K. Ye, H. Zhang, *Adv. Mater.* **2024**, *36*, 2311762.
[21] C. Yang, B. Zhuang, J. Lin, S. Wang, M. Liu, N. Jiang, D. Chen, *Chem. Eng. J.* **2020**, *398*, 125616.
[22] X. Zhang, L. Guo, Y. Zhang, C. Cheng, Y. Cheng, X. Li, J. Zhang, S. Xu, Y. Cao, B. Chen, *J. Non-Cryst. Solids* **2020**, *541*, 120066.
[23] K. Oreshkina, V. Dubrovin, Y. Sgibnev, N. Nikonorov, A. Babkina, E. Kulpina, A. Pavliuk, K. Zyryanova, A. Ignatiev, N. Kuzmenko, R. Kharisova, V. Klinkov, E. Zhizhin, A. Koroleva, N. Platonova, *Mater. Res. Bull.* **2022**, *149*, 111720.
[24] Y. Liu, J. Wang, J. Han, C. Liu, J. Ruan, *J. Am. Ceram. Soc.* **2022**, *105*, 7228.
[25] Y. Lu, Y. Xu, S. Chen, J. Lin, J. Zhu, S. Wang, Y. Zheng, F. Huang, D. Chen, *J. Lumin.* **2022**, *248*, 118952.
[26] C. Lin, D. Chen, K. Weng, Q. Jiao, J. Ren, S. Dai, *J. Phys. Chem. Lett.* **2020**, *11*, 6084.
[27] R. Zheng, J. Ueda, K. Shinozaki, S. Tanabe, *Chem. Mater.* **2022**, *34*, 1599.
[28] G. N. Greaves, A. Fontaine, P. Lagarde, D. Raoux, S. J. Gurman, *Nature* **1981**, *293*, 611.
[29] M. Fortino, A. Berselli, N. Stone-Weiss, L. Deng, A. Goel, J. Du, A. Pedone, *J. Am. Ceram. Soc.* **2019**, *102*, 7225.
[30] O. Majérus, L. Cormier, G. Calas, B. Beuneu, *Phys. Rev. B* **2003**, *67*, 024210.
[31] L. Pedesseau, S. Ispas, W. Kob, *Phys. Rev. B* **2015**, *91*, 134201.
[32] E. Cao, Y. Yang, B. Hassan, I. Khan, D. Zhou, J. Qiu, *Ceram. Int.* **2024**, *50*, 28419.
[33] E. Cao, Y. Yang, B. Hassan, D. Zhou, J. Qiu, *Ceram. Int.* **2024**, *50*, 10183.
[34] Z. Yang, H. Zhang, Z. Fang, J. Yi, P. Song, X. Yu, D. Zhou, J. Qiu, X. Xu, *Chem. Eng. J.* **2022**, *427*, 131379.
[35] R. E. Youngman, M. J. Dejneka, *J. Am. Ceram. Soc.* **2002**, *85*, 1077.
[36] G. Lakshminarayana, E. M. Weis, B. L. Bennett, A. Labouriau, D. J. Williams, J. G. Duque, M. Sheik-Bahae, M. P. Hehlen, *Opt. Mater.* **2012**, *35*, 117.
[37] M. Tashiro, S. Sukenaga, S. Kawanishi, Y. Sato, Y. Takakuwa, H. Shibata, *J. Am. Ceram. Soc.* **2020**, *103*, 5139.
[38] V. G. Antunes, C. A. Figueroa, F. Alvarez, *Appl. Surf. Sci.* **2018**, *448*, 502.
[39] R. Zhang, Z. Zhou, X. Li, T. Pang, T. Song, H. Wu, Q. Liao, Z. Wang, F. Huang, K. Wu, D. Chen, *ACS Nano* **2025**, *19*, 14318.
[40] B. Yang, S. Mei, H. He, Y. Zhu, R. Hu, J. Zou, G. Xing, R. Guo, *J. Eur. Ceram. Soc.* **2022**, *42*, 258.
[41] S. Zhou, Q. Guo, H. Inoue, Q. Ye, A. Masuno, B. Zheng, Y. Yu, J. Qiu, *Adv. Mater.* **2014**, *26*, 7966.
[42] C. Luo, C. Yan, W. Li, F. Chun, M. Xie, Z. Zhu, Y. Gao, B. Guo, W. Yang, *Adv. Funct. Mater.* **2020**, *30*, 2000026.